Solar Energy Materials & Solar Cells 263 (2023) 112570

Contents lists available at ScienceDirect

Solar Energy Materials and Solar Cells

journal homepage: www.elsevier.com/locate/solmat

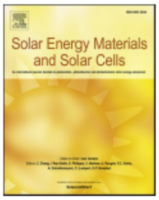

High-performance thermochromic YSZ/$V_{0.986}W_{0.014}O_2$/YSZ coatings for energy-saving smart windows

Michal Kaufman [a], Jaroslav Vlček [a,*], Jiří Houška [a], Radomír Čerstvý [a], Sadoon Farrukh [a], Mohamed Chargaoui [a], Stanislav Haviar [a], Jiechao Jiang [b], Efstathios I. Meletis [b], Šimon Kos [a]

[a] Department of Physics and NTIS-European Centre of Excellence, University of West Bohemia, Univerzitní 8, 30614, Plzeň, Czech Republic
[b] Department of Materials Science and Engineering, The University of Texas at Arlington, Arlington, 76019, TX, USA

ARTICLE INFO

Keywords:
Vanadium dioxide
Strongly thermochromic coatings
Low transition temperature
Pulsed magnetron sputtering
Low deposition temperature
Smart windows

ABSTRACT

The reversible semiconductor-to-metal transition of vanadium dioxide (VO_2) makes VO_2-based coatings a promising candidate for thermochromic smart windows, reducing the energy consumption of buildings. We report on a scalable sputter deposition technique for fast preparation of strongly thermochromic YSZ/$V_{0.986}W_{0.014}O_2$/YSZ coatings, where YSZ denotes Y-stabilized ZrO_2, on conventional soda-lime glass at a relatively low substrate surface temperature (350 °C) and without any substrate bias voltage. The thermochromic $V_{0.986}W_{0.014}O_2$ layers and the antireflection YSZ layers were deposited using a controlled high-power impulse magnetron sputtering of a single V–W and Zr–Y target, respectively. A coating design utilizing a second-order interference in the YSZ layers was applied to increase both the integral luminous transmittance (T_{lum}) and the modulation of the solar energy transmittance (ΔT_{sol}). We present the phase composition (X-ray diffraction) and microstructure (high-resolution transmission electron microscopy) of the coatings and their optical properties (spectrophotometry and spectroscopic ellipsometry). The YSZ/$V_{0.986}W_{0.014}O_2$/YSZ coatings exhibit a transition temperature of 33–35 °C with $T_{lum} = 64.5\%$ and $\Delta T_{sol} = 7.8\%$ for a $V_{0.986}W_{0.014}O_2$ thickness of 37 nm, and $T_{lum} = 46.1\%$ and $\Delta T_{sol} = 13.2\%$ for a $V_{0.986}W_{0.014}O_2$ thickness of 67 nm. The results constitute an important step to a cost-effective and high-rate preparation of large-area thermochromic VO_2-based coatings for future smart-window applications.

1. Introduction

Global warming and energy crisis drive a focus on energy-saving materials. Owing to the excessive use of heating, cooling, lighting and ventilation, buildings have been estimated to produce about 20% of all anthropogenic greenhouse gas emissions [1] and are responsible for up to 40% of the primary energy consumption [2] in the world. It is evident that energy-saving smart windows with adjustable throughput of solar energy can lower the energy expenditure.

Vanadium dioxide (VO_2) exhibits a reversible phase transition from a low-temperature monoclinic VO_2 (M1) semiconducting phase to a high-temperature tetragonal VO_2 (R) metallic phase at a transition temperature (T_{tr}) of approximately 68 °C for the bulk material [3]. The T_{tr} can be lowered using doping of VO_2 by other elements (such as W [4,5]). The automatic (i.e., without any switch system) response to temperature and the abrupt decrease of infrared transmittance without attenuation of luminous transmittance at the transition into the metallic state (effective utilization of daylight) make VO_2-based coatings a promising candidate for thermochromic smart windows reducing the energy consumption of buildings.

Magnetron sputter deposition with its versatility and the ease of scaling up to large substrate sizes is probably the most important preparation technique of thermochromic VO_2-based coatings [6–9]. Note that magnetron sputter sources are used very frequently not only in glass production lines (e.g., for deposition of low-emissivity coatings) but also in large-scale roll-to-roll deposition devices [10–12] producing coatings on ultrathin (0.02–0.20 mm) flexible glass or polymer foils.

To meet the requirements for large-scale implementation on building glass (glass panes, or flexible glass and polymer foils laminated to glass panes), VO_2-based coatings should satisfy the following strict criteria simultaneously: a maximum substrate temperature (T_s) during the preparation (deposition and possible post-annealing) close to 300 °C or lower [6,7,13,14], T_{tr} close to 20 °C [15], an integral luminous transmittance $T_{lum} > 60\%$ [16–18], a modulation of the solar energy

---

* Corresponding author.
E-mail address: vlcek@kfy.zcu.cz (J. Vlček).

https://doi.org/10.1016/j.solmat.2023.112570
Received 27 June 2023; Received in revised form 1 September 2023; Accepted 24 September 2023

transmittance $\Delta T_{sol} > 10\%$ [19–21], long-term environmental stability [8,22–24], and a more appealing color [25,26] than usual yellowish or brownish colors in transmission (smart window as seen from the inside).

However, usual approaches in the literature [8,16,27–31] are focused on the optimization of T_{lum} and ΔT_{sol} regardless of T_s and T_{tr}, lowering T_s using substrate bias voltage at the cost of making the deposition process significantly less industry-friendly, lowering T_{tr} using doping of VO_2 by other elements at the cost of much lower ΔT_{sol}, or choosing the thickness of antireflection (AR) layers (both below and above thermochromic VO_2-based layer) to optimize only T_{lum} (typically utilizing the first-order interference maximum) regardless of ΔT_{sol}. Moreover, most studies about deposition of VO_2 films are limited to experimental substrates (such as fused silica) and the transition to regular soda-lime window glass is still a challenge due to the problems with sodium diffusion.

Reactive high-power impulse magnetron sputtering (HiPIMS) is a promising scalable deposition technique for a low-temperature (300–350 °C) preparation of thermochromic VO_2-based films. Recently, valuable results concerning the low-temperature HiPIMS depositions of undoped thermochromic VO_2 films have been presented [13,14,18,22,32,33]. For example, a significantly higher environmental stability of the VO_2 films prepared using HiPIMS than using a conventional radio frequency (RF) magnetron sputtering was proved [22]. Here, it should be mentioned that HiPIMS techniques have the advantage of using essentially conventional magnetron sputtering equipment, while only replacing the power supply operating at a similar (not high) average power. Thus, these techniques can be implemented into large-scale deposition devices with various target geometries [34] (for example, with new rotatable targets).

In our recent paper [35], we presented a scalable deposition technique used for a low-temperature preparation of high-performance $ZrO_2/V_{0.982}W_{0.018}O_2/ZrO_2$ coatings on soda-lime glass (SLG). The thermochromic $V_{0.982}W_{0.018}O_2$ layers were deposited by controlled standard (the voltage pulse duration of 50 μs) HiPIMS of a V target, combined with a simultaneous pulsed DC magnetron sputtering of a W target (doping of VO_2 by W to reduce the transition temperature to T_{tr} = 20–21 °C without any degradation of thermochromic properties), at T_s = 330 °C in an argon-oxygen gas mixture. A simple, but very effective, pulsed oxygen flow control made it possible to deliver a high power into discharge pulses with a minimized microarcing on the target surface and thus, to utilize two exclusive benefits of the reactive HiPIMS [36,37]. The first benefit is highly ionized fluxes of particles with many V^+ and V^{2+} ions onto the substrate, and enhanced energies and momenta of the ions bombarding the growing W-doped VO_2 layers, allowing us to achieve the crystallinity of the thermochromic VO_2 phase in them at the low T_s = 330 °C and without any substrate bias voltage. The second benefit is a very high degree of dissociation of the O_2 molecules injected into the high-density plasma in front of the V target, allowing us to achieve the required VO_2 stoichiometry at a low compound (oxide) fraction in the target surface layer. This is of key importance for process stability (reduced microarcing on the target), for increased sputtering of V atoms and for low production of O^- ions at the target [38]. A coating design utilizing a second-order interference in the ZrO_2 AR layers was applied to increase both T_{lum} and ΔT_{sol} [39]. The $ZrO_2/V_{0.982}W_{0.018}O_2/ZrO_2$ coatings exhibited T_{lum} = 59.4% and ΔT_{sol} = 5.5% for a $V_{0.982}W_{0.018}O_2$ thickness of 45 nm, and T_{lum} = 48.0% and ΔT_{sol} = 10.4% for a $V_{0.982}W_{0.018}O_2$ thickness of 69 nm.

In our preceding paper [40], we reported on successful transfer of this sputter technique for deposition of three-layer strongly thermochromic ZrO_2/W-doped VO_2/ZrO_2 coatings on ultrathin (0.1 mm) flexible glass from a laboratory-scale device with three (V, W and Zr) planar magnetron targets to a large-scale roll-to-roll device with two (W-doped V and ZrO_2) rotatable magnetron targets. The thermochromic W-doped VO_2 layers were prepared using a controlled standard (the voltage pulse duration of 70–80 μs) HiPIMS at a deposition-averaged target power density of 10–14 W cm^{-2} in both deposition devices.

In this paper, we report on a scalable sputter deposition technique for the preparation of strongly thermochromic YSZ/$V_{0.986}W_{0.014}O_2$/YSZ coatings, where YSZ denotes the Y-stabilized ZrO_2, on conventional SLG at T_s = 350 °C and without any substrate bias voltage. The thermochromic $V_{0.986}W_{0.014}O_2$ layers were deposited using a controlled deep oscillation magnetron sputtering (DOMS) of a single V–W target while the YSZ AR layers were deposited using a controlled standard HiPIMS of a single Zr–Y target. Here, it should be mentioned that the use of only two composite targets is desirable for preparation of three-layer thermochromic VO_2-based coatings in large-scale deposition devices [40]. The DOMS is a modified version of HiPIMS with packages (macropulses) of short high-power micropulses [41,42]. Our motivation to apply this high-power discharge with short voltage pulses was to further increase discharge stability during the deposition by minimizing the number of microarcs on the V–W target and to utilize a different energetics of the reactive deposition process (particularly at the higher deposition-averaged target power density used, resulting in a high deposition rate of the $V_{0.986}W_{0.014}O_2$ layers) compared with that during a standard HiPIMS deposition. Our motivation to apply the YSZ AR layers instead of the ZrO_2 AR layers was to further improve the crystallinity of the thermochromic VO_2 phase in the $V_{0.986}W_{0.014}O_2$ layers, as the bottom AR layers provide also a structure template for their growth. In addition to the VO_2 stoichiometry, the microstructure (particularly the degree of crystallinity and the size and orientation of the W-doped VO_2 crystal grains) of the $V_{0.986}W_{0.014}O_2$ layer is very important for the thermochromic performance (including ΔT_{sol}) of coatings. A key importance of the microstructure of undoped VO_2 films for a strong and sharp semiconductor-to-metal transition was shown when they grew epitaxially on sapphire substrate (≈200 nm thick VO_2 films with a lateral size of the VO_2 crystal grains larger than 150 nm [43]) and on YSZ substrate [44].

The main aim of this study is to present the design, phase composition and microstructure, and optical properties of these high-performance durable three-layer thermochromic VO_2-based coatings with a low transition temperature T_{tr} = 33–35 °C, and to explain the fundamental principles of the novel scalable deposition technique for their fast preparation on conventional SLG at a low T_s = 350 °C.

2. Experimental details

2.1. Deposition process

The $V_{0.986}W_{0.014}O_2$ layers were deposited using a strongly unbalanced magnetron source [45] with a directly water-cooled single V–W (4.0 wt% corresponding to 1.14 at.%) target (99.95% purity, diameter of 100 mm and thickness of 6 mm) in a standard stainless-steel vacuum chamber (diameter of 507 mm and length of 520 mm), which was evacuated by a diffusion pump (2 m^3s^{-1}) backed up with a rotary pump (30 m^3h^{-1}). The base pressure before deposition was 10^{-3} Pa. The substrates (12 × 25 mm^2) at the distance of 100 mm from the target were at a floating potential. The substrate surface temperature, maintained during the deposition by a built-in heating system, was 350 °C.

The magnetron was driven by a DOMS power supply (HIPIMS Cyprium plasma generator, Zpulser Inc.). In this work, the macropulse (composed of 10 micropulses) duration was 500 μs at a repetition frequency of 640 Hz. The micropulse on-time was 26 μs at a repetition frequency of 20 kHz within a macropulse (see Fig. 1). The deposition-averaged target power density (averaged over the total target area) was approximately 34 Wcm^{-2}.

Oxygen was admitted into the vacuum chamber via mass flow controller and two corundum conduits. Two O_2 inlets with a diameter of 1 mm were placed symmetrically above the V–W target racetrack at the same distance of 20 mm from the V–W target surface and oriented to the substrate. The to-substrate O_2 injection into the dense plasma in front of the sputtered target is very suitable for reactive HiPIMS depositions of oxide films [46]. It leads to a substantially (2–3 times [46]) increased

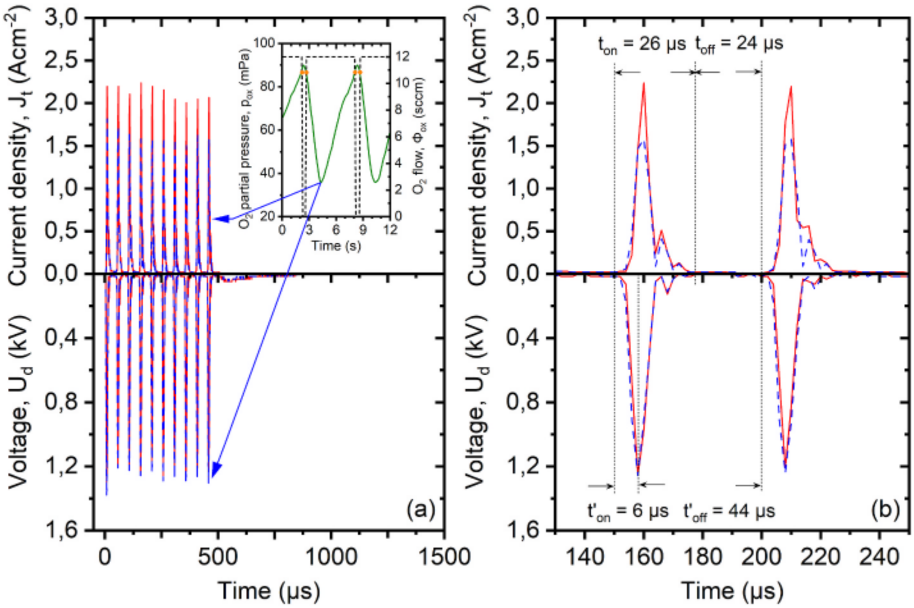

Fig. 1. Waveforms of the magnetron voltage (U_d) and the target current density (J_t) for a 500 μs macropulse composed of 10 micropulses (panel a) and for a micropulse with the pulse-on time $t_{on} = 26\ \mu s$ (panel b) during a deposition of the thermochromic $V_{0.986}W_{0.014}O_2$ layers (Fig. 2) at a deposition-averaged target power density close to 34 Wcm^{-2}. Time evolution of the oxygen partial pressure (p_{ox}) during the deposition is shown in the inset of panel a. A pre-selected critical value $(p_{ox})_{cr} = 87$ mPa determining the switching-on and switching-off of the oxygen flow rate $\Phi_{ox} = 12$ sccm is marked by dots. In the main panels, the dashed (blue) and full (red) lines represent the waveforms (both U_d and J_t) measured at the minimum (indicated in panel a) and maximum p_{ox} during the deposition, respectively. The micropulse voltage-on time $t'_{on} = 6\ \mu s$ and the voltage-off time $t'_{off} = 44\ \mu s$ as defined by the power-supply software are given in panel b.

local oxygen partial pressure in front of the O_2 inlets, compared with the oxygen partial pressure (p_{ox}) in the vacuum chamber, at a very high degree of dissociation of O_2 molecules in the high-density plasma in front of the target. As a consequence, the p_{ox} needed for preparation of stoichiometric VO_2 layers can be very low, resulting in the required (for process stability, for increased sputtering of V and W atoms, and for low production of high-energy O^- ions) low compound (oxide) fraction in the target surface layer.

The argon flow rate was 25 sccm corresponding to $p_{ar} = 0.5$ Pa, while the total oxygen flow rate (Φ_{ox}) in both conduits was not fixed but alternating between 0 and 12 sccm (see Fig. 1). The moments of switching of the Φ_{ox} pulses were determined during the deposition by a programmable logic controller using a pre-selected critical value of the oxygen partial pressure $(p_{ox})_{cr} = 87$ mPa: when $p_{ox}(t) < (p_{ox})_{cr}$, $\Phi_{ox} = 12$ sccm and when $p_{ox}(t) \geq (p_{ox})_{cr}$, $\Phi_{ox} = 0$ sccm. The values of p_{ar} and of $p_{ar} + p_{ox}$ were measured at the chamber wall using a high stability capacitance manometer (Baratron, Type 127, MKS) with the accuracy much better than 1%.

The used controlled sputter deposition technique made possible a fast synthesis (53 nm/min) of the $V_{0.986}W_{0.014}O_2$ layers with a highly crystalline thermochromic VO_2 phase on unbiased substrates (YSZ layers on 1 mm thick SLG) at $T_s = 350$ °C. The fundamental principle of this technique is presented in Fig. 1, which shows the time evolution of the voltage ($U_d(t)$) and the target current density ($J_t(t)$), averaged over the total target area, during a deposition of the $V_{0.986}W_{0.014}O_2$ layer. As can be seen in Fig. 1, the waveforms of $U_d(t)$ and $J_t(t)$ oscillate in a dependence on the value of p_{ox}, being in the range from 33 mPa to 92 mPa (see Fig. 1a). The corresponding maximum target power densities in a micropulse were 2100 Wcm^{-2} and 2600 Wcm^{-2}, respectively. These values are not equal to the product of the maximum $|U_d|$ and the maximum J_t owing to a delay in the maximum J_t compared to the maximum $|U_d|$. Let us recall that, in contrast with commonly used, more complex, control systems, the pulsed oxygen flow control does not try to keep a pre-selected constant value of p_{ox} during the deposition but it allows for a pre-selected interval of p_{ox}. This is of key importance for process stability, as we have no problems with inertia of the inlet system, delay of valves and sensors, and hysteresis effects. The asymmetry in the $p_{ox}(t)$ dependence presented in the inset of Fig. 1a is mainly due to a fast closing and delayed opening of the O_2 mass flow controller at the relatively low $\Phi_{ox} = 12$ sccm and a fast sputtering of the V (and W) atoms from the target.

A detailed characterization of the complicated chemical and physical processes on the sputter V–W target, in the discharge plasma and on the surface of growing W-doped VO_x layers, which determine the elemental composition, structure and thermochromic properties of the layers produced using this controlled deposition technique, are given in Ref. [47].

The bottom and the top YSZ AR layers (see Fig. 2) were deposited using a controlled standard HiPIMS onto substrates held at a floating potential with the substrate surface temperature of 350 °C and below 60 °C (without any external heating), respectively. The lower deposition temperature for the top AR layers was used to avoid oxidation of the thermochromic $V_{0.986}W_{0.014}O_2$ layers, as the preparation of the whole three-layer YSZ/$V_{0.986}W_{0.014}O_2$ / YSZ coatings was not performed in the same vacuum chamber. An unbalanced magnetron with a single Zr–Y (9.0 wt% corresponding to 9.2 at.%) target (99.9% purity, diameter of 50 mm and thickness of 6 mm) was driven by a unipolar high-power pulsed DC power supply (TruPlasma Highpulse 4002 TRUMPF Huettinger) at $p_{ar} = 1$ Pa and the p_{ox} oscillating between 25 mPa and 73 mPa. In this work, the voltage pulse duration was 80 μs at a repetition frequency of 500 Hz (duty cycle of 4%) and the deposition-averaged target power density was 14 Wcm^{-2}. The target-to-substrate distance was 145 mm.

2.2. Coating characterization

The W content in the metal sublattice of $V_{0.986}W_{0.014}O_2$, i.e., 1.4 ±0.2 at.%, was measured on a dedicated 800 nm thick layer on Si(100) substrate in a scanning electron microscope (SU-70, Hitachi) using wave-dispersive spectroscopy (Magnaray, Thermo Scientific) at a low primary electron energy of 7.5 keV. The higher thickness of the dedicated layer and the low primary electron energy collectively facilitate

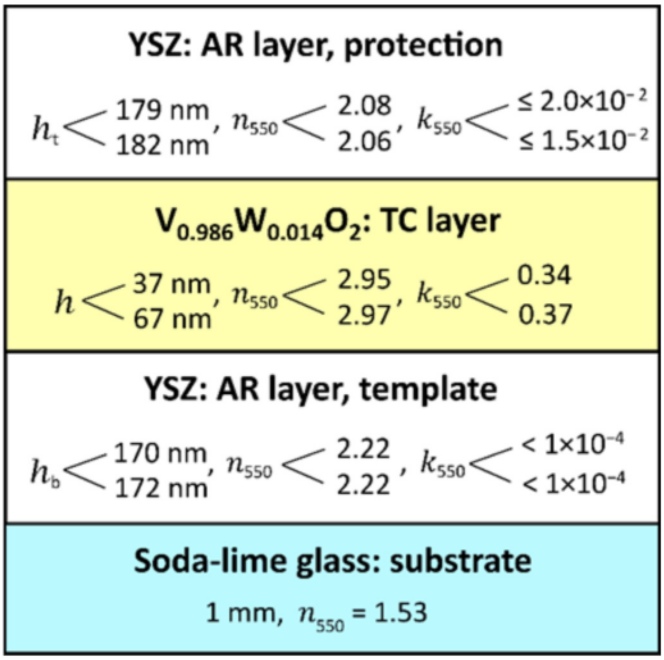

Fig. 2. The three-layer thermochromic VO_2-based coatings on a soda-lime glass substrate investigated in this paper (not in scale; see TEM in Fig. 3 for a figure which is in scale). Here, h_b, h and h_t represent the thickness of the bottom YSZ layer, the thickness of the thermochromic $V_{0.986}W_{0.014}O_2$ layer, and the thickness of the top YSZ layer, respectively. The refractive index (n_{550}) and extinction coefficient (k_{550}) at the wavelength of 550 nm of all layers were measured at $T_m = 23°C$.

using the bulk procedure for processing the data. Standard reference samples for pure V, W and Fe_2O_3 (Astimex Scientific Ltd.) were utilized. The room-temperature crystal structure of both $V_{0.986}W_{0.014}O_2$ and YSZ was characterized by X-ray diffraction (XRD) using a PANanalytical X'Pert PRO diffractometer working with a CuKα (40 kV, 40 mA) radiation at a glancing incidence of 1°. The average size of coherently diffracting regions of the VO_2 (M1)/VO_2 (R) phase was estimated from the corrected full width at half maximum of the main VO_2 (M1)/VO_2 (R) diffraction peak using the Scherrer equation. At first, the diffraction peak was approximated by pseudo-Voigt function. Then, the calculated value of the full width at half maximum was corrected for instrumental broadening using a LaB_6 powder standard. The fine microstructure of the YSZ/$V_{0.986}W_{0.014}O_2$/YSZ coating was investigated by transmission electron microscopy (TEM). Cross-section TEM samples were prepared by mechanical grinding and polishing, followed by dimpling using a Gatan Model 656 dimple grinder and Ar-ion milling in a Gatan Model 691 precision ion polishing system. Selected-area electron diffraction (SAED) patterns, and TEM and HRTEM images were recorded in a Hitachi H-9500 electron microscope that is attached with a Gatan SC-1000 Orius CCD camera (4008 × 2672 pixels). The microscope was operated at 300 keV with a lattice resolution of 1 Å.

The thickness and room-temperature optical constants (refractive index, n, and extinction coefficient, k) of individual layers were measured by spectroscopic ellipsometry. The exactness has been enhanced by characterizing each of the three layers separately, before the deposition of the next one and assuming fixed properties of the layer (s) below it. The transmittance (T) and reflectance (R) were measured by spectrophotometer equipped by an in-house made heat/cool cell. The measurement temperature (T_m) was varied between $T_{ms} = -20$ °C and $T_{mm} = 70$ °C (between the semiconducting and the metallic state of the $V_{0.986}W_{0.014}O_2$ layer, respectively).

The coating performance is quantified by means of integral luminous transmittance, reflectance and absorption (T_{lum}, R_{lum} and A_{lum}, respectively), their modulations (ΔT_{lum}, ΔR_{lum} and ΔA_{lum}), integral solar energy transmittance, reflectance and absorption (T_{sol}, R_{sol} and A_{sol}, respectively) and again their modulations (ΔT_{sol}, ΔR_{sol} and ΔA_{sol}). The quantities are defined as

$$T_{lum}(T_m) = \frac{\int_{380}^{780} \varphi_{lum}(\lambda)\varphi_{sol}(\lambda)T(T_m,\lambda)\mathrm{d}\lambda}{\int_{380}^{780} \varphi_{lum}(\lambda)\varphi_{sol}(\lambda)\mathrm{d}\lambda}, \tag{1}$$

$$\Delta T_{lum} = T_{lum}(T_{ms}) - T_{lum}(T_{mm}), \tag{2}$$

$$T_{sol}(T_m) = \frac{\int_{300}^{2500} \varphi_{sol}(\lambda)T(T_m,\lambda)\mathrm{d}\lambda}{\int_{300}^{2500} \varphi_{sol}(\lambda)\mathrm{d}\lambda}, \tag{3}$$

$$\Delta T_{sol} = T_{sol}(T_{ms}) - T_{sol}(T_{mm}), \tag{4}$$

and similarly for R and A, where φ_{lum} is the luminous sensitivity of human eye and φ_{sol} is the solar irradiance spectrum [48]. The presented T_{lum} is equal to $[T_{lum}(T_{ms}) + T_{lum}(T_{mm})]/2$.

3. Results and discussion

3.1. Coating design

The overall idea behind the design of the presented coatings is indicated by referring to them as YSZ/$V_{0.986}W_{0.014}O_2$/YSZ, see Fig. 2 (design itself) and Fig. 3 (example of its successful realization). In order to demonstrate the trade-off between T_{lum} and ΔT_{sol}, the design has been realized at two different thicknesses of the thermochromic (TC) layer: h = 37 nm and 67 nm (values inside the range where this trade-off takes place [31]). The qualitative benefits of this design include: (i) the aforementioned growth template role of the bottom YSZ layer, (ii) a protective role (against both mechanical and chemical damage) of the top YSZ layer, and (iii) an antireflection role of both YSZ layers. In order to fully utilize the third role and to optimize (at a given h) T_{lum} as well as ΔT_{sol}, the design has to be properly quantified.

First, the achievable transmittance (upper envelope of the interference curve) is maximized when the AR layer has its refractive index between (in a first approximation ideally the geometric mean) those of the materials around it. The numbers in Fig. 2 confirm that this requirement is well fulfilled by the AR layers used: n_{550} of the bottom YSZ (2.22) is between n_{550} of the TC layer (2.95–2.97 below T_{tr}) and n_{550} of glass (1.53), and n_{550} of the top YSZ (2.06–2.08) is between n_{550} of the TC layer (2.95–2.97) and n_{550} of air (1.00). Note that lowering the deposition temperature of the top YSZ layer is beneficial not only because it makes the process more industry-friendly, but also because the consequently lowered n_{550} approaches its ideal value. Second, the AR layers should be as transparent as possible. This is completely

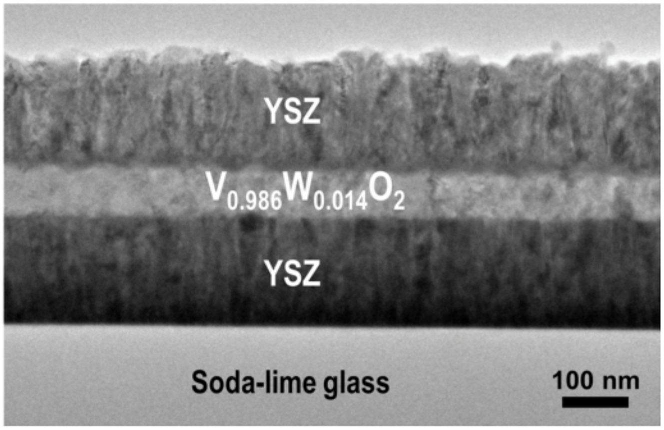

Fig. 3. Cross-section TEM image of the YSZ (172 nm)/$V_{0.986}W_{0.014}O_2$ (67 nm)/YSZ (182 nm) coating on 1 mm thick soda-lime glass substrate.

fulfilled by the bottom YSZ ($k_{550} < 10^{-4}$), and largely fulfilled by the top YSZ ($k_{550} \leq 1.5$-2.0×10^{-2}). Nevertheless, the finite k_{550} of the top YSZ (prepared at a lower temperature and on a different template than the bottom YSZ) probably lowers T_{lum} by 3% (at $h = 67$ nm) to 6% (at $h = 37$ nm). In other words, the presented pairs of T_{lum} and ΔT_{sol} constitute, despite being kind of record, a lower bound of the potential of the presented coating design and deposition technique. Third, T_{lum} is maximized when T(λ) approaches its upper envelope around $\lambda = 550$ nm. This is achieved by proper thickness of the AR layers, in the first approximation $\lambda/4\ n_{550}$ (first-order maximum), $3\lambda/4\ n_{550}$ (second-order maximum), etc. The key thing to note is that while the first-order maximum in the visible does not lead to anything special in the infrared, the second-order maximum in the visible leads to a first-order maximum in the infrared where most of the energy saving takes place. Higher T(λ) in the infrared leads to its higher modulation and in turn to higher ΔT_{sol} at about the same T_{lum} (shown graphically in Ref. [39]). The YSZ thicknesses leading to the second-order interference maximum in the visible have been optimized using measured properties of individual layers and an in-house code based on the transfer matrix formalism. In particular, second-order AR layers with thicknesses $h_b =$ 170–172 nm (bottom YSZ) and $h_t =$ 179–182 nm (top YSZ; the product of higher thickness and lower n_{550} leads to the same optical path length) have been utilized.

3.2. Phase composition and microstructure

The XRD patterns of the bottom YSZ (172 nm) AR layer, of the two-layer thermochromic YSZ (172 nm)/$V_{0.986}W_{0.014}O_2$ (67 nm) coating, and the three-layer thermochromic YSZ (172 nm)/$V_{0.986}W_{0.014}O_2$ (67 nm)/YSZ (182 nm) coating are shown in Fig. 4. As can be seen, the YSZ AR layers are well crystalline, see the strong narrow peaks close to the reported positions of a tetragonal $Y_{0.06}Zr_{0.94}O_{1.97}$ phase (PDF # 04-021-9607 [49]). This confirms the aforementioned second role of the bottom AR layer as a structure template improving the crystallinity of the thermochromic W-doped VO_2 layer. Regarding the thermochromic $V_{0.986}W_{0.014}O_2$ layer, the most important piece of information is that there are not detected any contributions from undesired non-thermochromic polymorphs, such as VO_2(B) or VO_2(P), and non-thermochromic phases with slightly different stoichiometries from VO_2, such as V_9O_{17} or V_6O_{13}. All peaks are identified as diffraction peaks of either the low-temperature monoclinic VO_2(M1) phase (PDF # 04-003-2035) or the high-temperature tetragonal VO_2 (R) phase (PDF # 01-073-2362). These two thermochromic phases are difficult to distinguish and they are actually expected to be present simultaneously because the measurement temperature $T_m = 25$ °C is close to the transition temperature $T_{tr} = 33$ °C of the investigated coating (as shown later). See, e.g., the strongest peak around $2\Theta = 27.8°$ corresponding well to theoretical positions of the VO_2 (M1)(011) planes and the VO_2 (R)(110) planes with $2\Theta = 27.80°$ and 27.91°, respectively. The size of coherently diffracting regions of the thermochromic VO_2 (M1)/VO_2 (R) phase, estimated from the width of this main VO_2 (M1)/VO_2 (R) diffraction peak, is 36 nm. Note that almost no difference in the size of coherently diffracting regions was observed for the $V_{0.986}W_{0.014}O_2$ layer with the thickness of 37 nm, but the accuracy of the estimation was decreased owing to a lower signal-to-noise ratio.

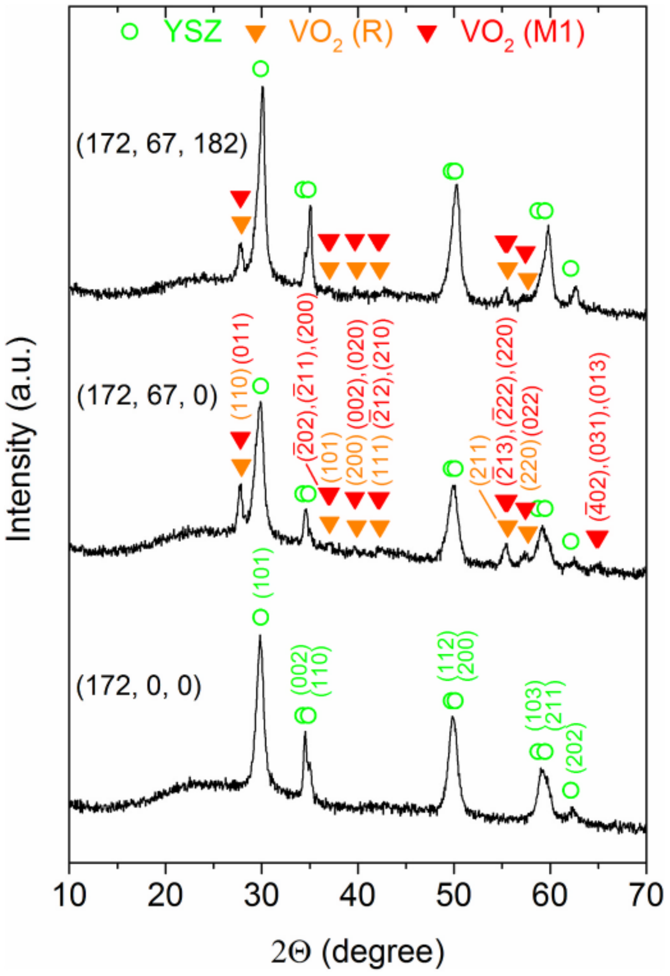

Fig. 4. X-ray diffraction patterns taken at $T_m = 25°C$ from the YSZ (172 nm)/$V_{0.986}W_{0.014}O_2$ (67 nm)/YSZ (182 nm) coating on a 1 mm thick glass substrate. For comparison, the X-ray diffraction patterns from the corresponding YSZ (172 nm) layer and YSZ (172 nm)/$V_{0.986}W_{0.014}O_2$ (67 nm) coating on the same substrate are given. The main diffraction peaks of VO_2 (R), VO_2 (M1) and YSZ (tetragonal $Y_{0.06}Zr_{0.94}O_{1.97}$) are marked.

Fig. 5 presents cross-section HRTEM images and a SAED pattern taken from the YSZ (172 nm)/$V_{0.986}W_{0.014}O_2$ (67 nm)/YSZ (182 nm) coating. As can be seen in Fig. 5a, the $V_{0.986}W_{0.014}O_2$ layer exhibits a compact crystal structure with different sizes and orientations of VO_2 crystal grains which are interconnected via amorphous nanodomains with a size of ~1–2 nm formed along the VO_2 grain boundaries. Note that a brighter contrast on the image represents a less dense material in the amorphous nanodomains and in some parts of the VO_2 grains. These amorphous nanodomains are narrower compared to those formed along the VO_2 grain boundaries in the thermochromic $V_{0.984}W_{0.016}O_2$ layer of ZrO_2/$V_{0.984}W_{0.016}O_2$/ZrO_2 coating [50], investigated in our recent paper (see the consequently improved quantified coating performance in the next section). The d-spacing of the lattice fringes related to the large crystal grain on the left side of the image (see Fig. 5a) is about 3.20 Å corresponding to the monoclinic VO_2 (M1)(011) planes [49] with d = 3.21 Å or the tetragonal VO_2 (R)(110) planes with d = 3.19 Å. Note that a vertical dimension of this crystal grain is much larger than 30 nm. The d-spacing of the lattice fringes related to the crystal grain on the bottom right is about 2.32 Å corresponding to the monoclinic VO_2 (M1)$(\bar{1}12)$ planes with d = 2.31 Å, and the d-spacing of the lattice fringes related to the crystal grain on the top right is about 2.15 Å closely corresponding to the monoclinic VO_2 (M1)$(\bar{2}12)$ planes with d = 2.15 Å or the tetragonal VO_2 (R)(111) planes with d = 2.14 Å (see agreement with Fig. 4). Fig. 5b shows the crystal structure of the bottom YSZ layer formed by tetragonal YSZ crystal grains. It is much more compact (very narrow amorphous boundary regions) than that of bottom ZrO_2 layer in the aforementioned ZrO_2/$V_{0.984}W_{0.016}O_2$/ZrO_2 coating [50] comprising monoclinic and tetragonal ZrO_2 crystal grains. The d-spacing of the lattice fringes related to most of the YSZ crystal grains in the image is about 2.98 Å corresponding to the YSZ (101) planes with the same d = 2.98 Å. The d-spacing of the lattice fringes related to the YSZ crystal grains on the top of the image is about 2.57 Å corresponding to the YSZ (110) planes with d = 2.57 Å and possibly (small contribution) also to the YSZ (002) planes with d = 2.61 Å (see Fig. 4). Fig. 5c presents a SAED pattern taken

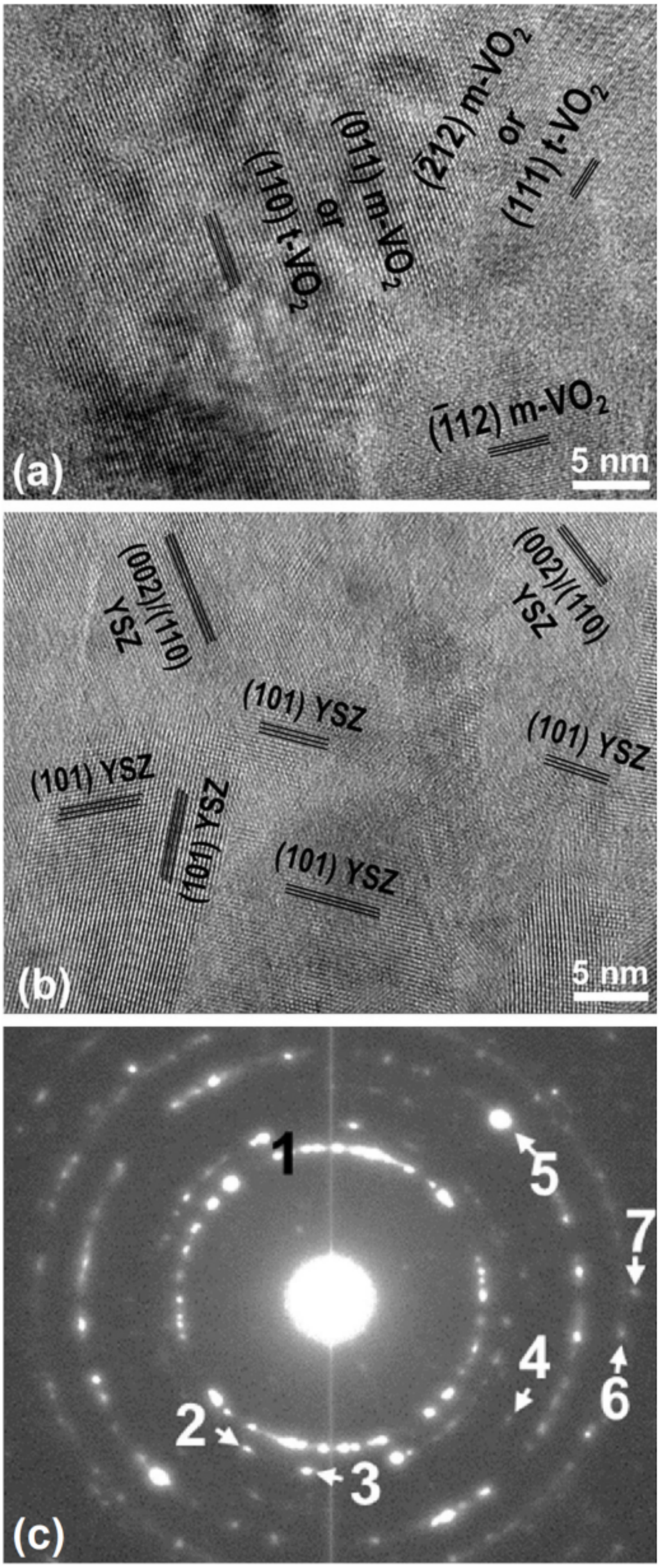

Fig. 5. Cross-section HRTEM images taken from central parts of the $V_{0.986}W_{0.014}O_2$ layer (a) and the bottom YSZ layer (b) in the YSZ (172 nm)/$V_{0.986}W_{0.014}O_2$ (67 nm)/YSZ (182 nm) coating on 1 mm thick glass substrate. SAED pattern taken from the bottom YSZ layer (c) with the d-spacings of the diffraction rings or spots 1, 2, 3, 4, 5, 6 and 7 equal to 2.98 Å, 2.61 Å, 2.57 Å, 2.12 Å, 1.82 Å, 1.57 Å and 1.48 Å, respectively.

from the YSZ layer shown in Fig. 5b. The d-spacings and intensities of the diffraction rings and spots match almost perfectly the diffraction in the PDF [49] of the tetragonal $Y_{0.06}Zr_{0.94}O_2$ phase (see the excellent agreement with Fig. 4). The diffraction rings 1 and 3 with the measured $d = 2.98$ Å and 2.57 Å, respectively, are related to the aforementioned YSZ (101) planes with the same $d = 2.98$ Å and YSZ (110) planes with $d = 2.57$ Å. The diffraction ring 5 with the measured $d = 1.82$ Å corresponds to a superposition of the YSZ (200) planes with $d = 1.82$ Å and the YSZ (112) planes with $d = 1.83$ Å, while the diffraction ring 6 with the measured $d = 1.57$ Å corresponds to a superposition of the YSZ (103) planes with d = 1.57 Å and the YSZ (211) planes with $d = 1.55$ Å. The diffraction spots 2, 4 and 7 with the measured $d = 2.61$ Å, 2.12 Å and 1.48 Å, respectively, are related to the YSZ (002) planes with the same $d = 2.61$ Å, the YSZ (102) planes with $d = 2.12$ Å (not observed in Fig. 4) and the YSZ (202) planes with $d = 1.49$ Å.

3.3. Thermochromic properties

The thermochromic performance of YSZ/$V_{0.986}W_{0.014}O_2$/YSZ coatings is quantified in terms of T_{tr} (Fig. 6), spectral quantities (Fig. 7) and integral quantities (Fig. 8 and Table 1). Fig. 6 shows that the usage of a single (i.e., industry-friendly) V–W target allowed us to incorporate W into the metal sublattice of VO_2 and to decrease T_{tr} from 56 to 57 °C (sputtering of pure VO_2 in the same device [36,37]) to 33–35 °C. This is still above the desired room temperature, partially due to the growth conditions during HiPIMS of the top YSZ layer: a preliminary analysis indicates that these conditions led not only to the suboptimum microstructure and k_{550} of YSZ, but also to an enhancement of T_{tr} by up to 5 °C. However, V–W targets of other compositions can be used in the future to achieve T_{tr} of ≈20 °C, similarly to what we already achieved [35] by sputtering V and W from two different targets. Other functional properties (arguably affected by the presence of crystals of different sizes in polycrystaline $V_{0.986}W_{0.014}O_2$) shown in Fig. 6 are the width of the middle section ($\approx 13°C$) and the total width of the hysteresis loop.

The spectral transmittance of YSZ/$V_{0.986}W_{0.014}O_2$/YSZ coatings is shown in Fig. 7a, which allows one to note numerous features. The first

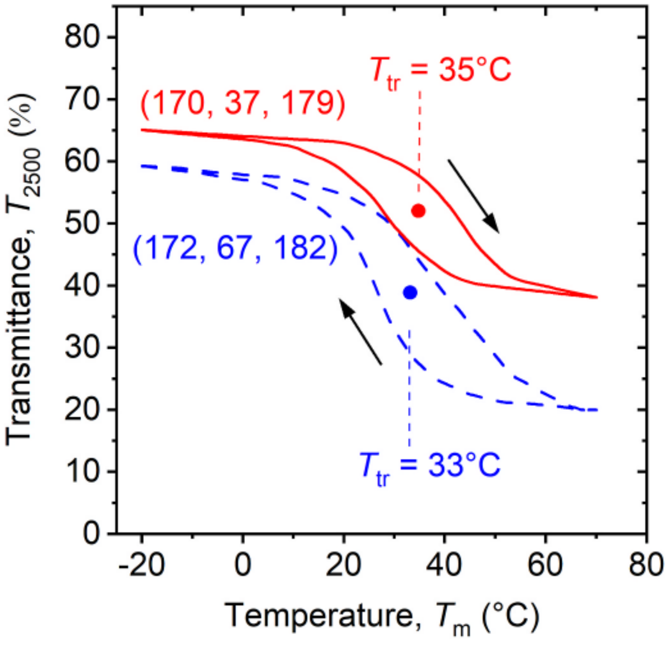

Fig. 6. Temperature (T_m) dependence of the transmittance (T_{2500}) at 2500 nm for the YSZ (170 nm)/$V_{0.986}W_{0.014}O_2$ (37 nm)/YSZ (179 nm) coating (full lines) and the YSZ (172 nm)/$V_{0.986}W_{0.014}O_2$ (67 nm)/YSZ (182 nm) coating (dashed lines) deposited onto 1 mm thick glass substrates (Fig. 2). The transition temperatures (T_{tr}) are also given.

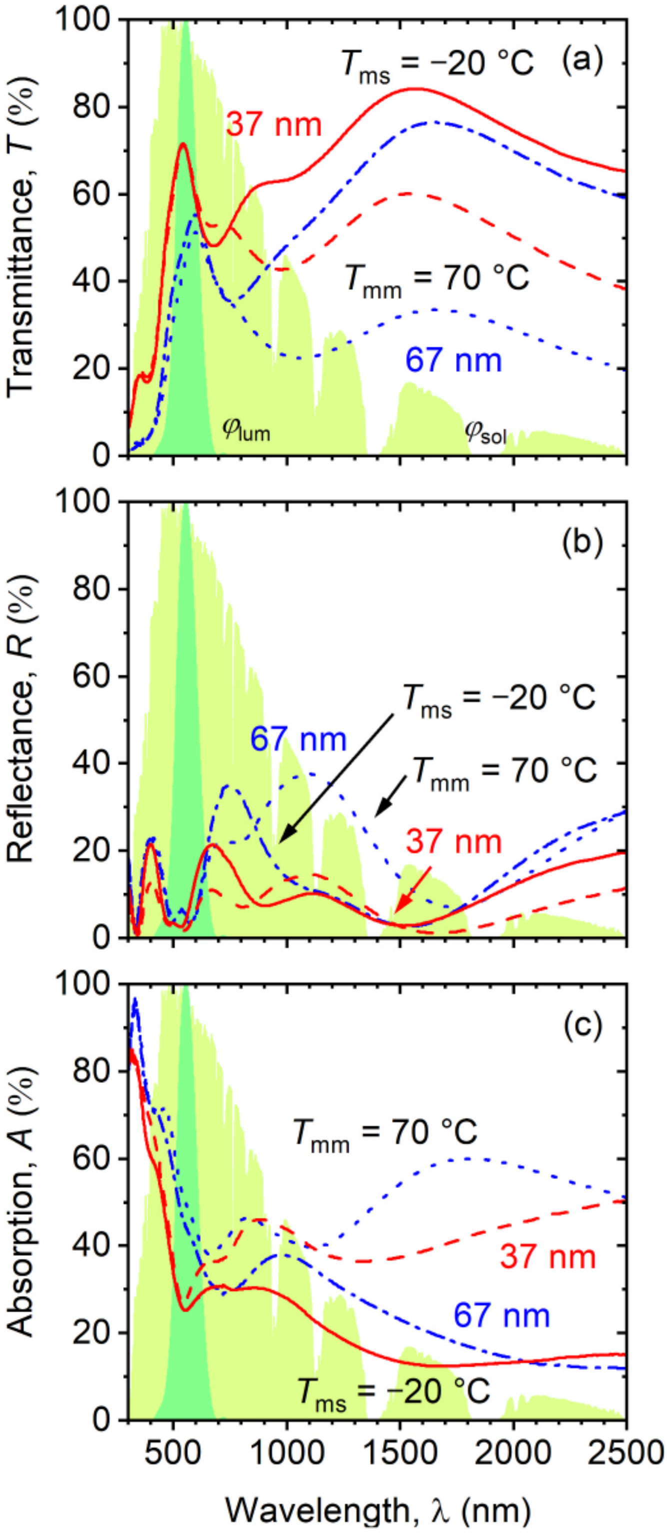

Fig. 7. Spectral (a) transmittance (T), (b) reflectance (R) and (c) absorption (A) at an angle of incidence of 7° for the YSZ (170 nm)/$V_{0.986}W_{0.014}O_2$ (37 nm)/YSZ (179 nm) coating (full and dashed lines) and the YSZ (172 nm)/$V_{0.986}W_{0.014}O_2$ (67 nm)/YSZ (182 nm) coating (dash-dotted and dotted lines) on 1 mm thick glass substrates at $T_{ms} = -20°C$ (full and dash-dotted lines) and $T_{mm} = 70°C$ (dashed and dotted lines). The contours of the shaded areas represent the luminous sensitivity of the human eye (φ_{lum}) and the sea-level solar irradiance spectrum at an air mass of 1.5 (φ_{sol}), normalized to maxima of 100%.

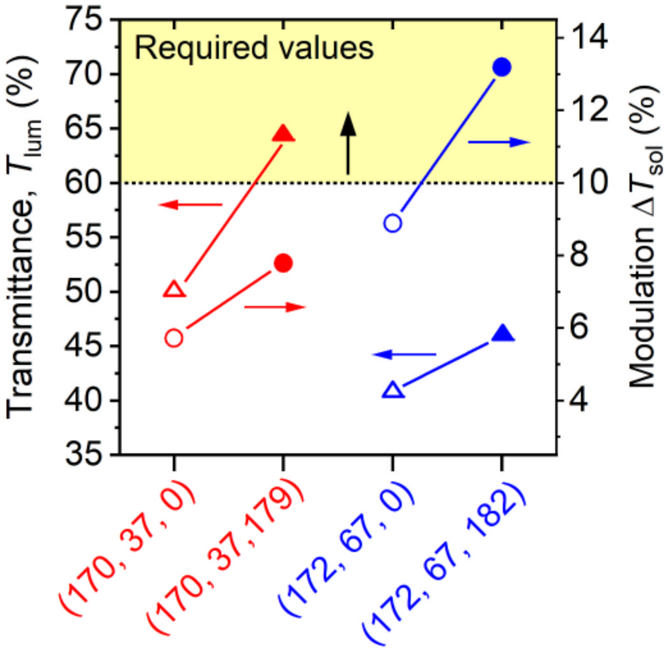

Fig. 8. The average luminous transmittance (T_{lum}) and the modulation of the solar energy transmittance (ΔT_{sol}) for the YSZ (170 nm)/$V_{0.986}W_{0.014}O_2$ (37 nm)/YSZ (179 nm) coating and the YSZ (172 nm)/$V_{0.986}W_{0.014}O_2$ (67 nm)/YSZ (182 nm) coating (full symbols) on 1 mm thick glass substrates. For comparison, the T_{lum} and ΔT_{sol} for the corresponding YSZ (170 nm)/$V_{0.986}W_{0.014}O_2$ (37 nm) coating and the YSZ (172 nm)/$V_{0.986}W_{0.014}O_2$ (67 nm) coating (empty symbols) on the same substrates are given. The shaded area represents the required values for smart-window applications.

of them is the nature of the thermochromic transition in itself: $T(\lambda)$ modulation in the infrared at almost preserved $T(\lambda)$ in the visible (a significant advantage over market-available electrochromic coatings). Second, there is the desired interference maximum in the visible, maximizing T_{lum}. Third, this second-order maximum in the visible is accompanied by a first-order maximum in the infrared (at roughly 3 times longer wavelength), leading to enhanced ΔT_{sol}. Fourth, there is the first fingerprint of the trade-off between T_{lum} (higher $T(\lambda)$ in the visible at $h = 37$ nm) and ΔT_{sol} (higher $T(\lambda)$ modulation in the infrared at $h = 67$ nm). Fig. 7b shows the spectral reflectance, and confirms the functionality of the AR layers (despite the only approximately optimum n of YSZ): the minima around ≈550 nm and ≈1600 nm approach zero. There is a complicated $R(\lambda)$ modulation outside the positions of these minima: combination of the facts that the transition from VO_2 (M1) to VO_2 (R) leads not only to enhanced k but in most of the wavelength range (except at the longest λ) also to lower n [51]. Fig. 7c shows the spectral absorption, i.e., the complement of $T(\lambda)$ and $R(\lambda)$ to 1. While the transition from VO_2 (M1) to VO_2 (R) leads to enhanced $A(\lambda)$ in most of the wavelength range, the most pronounced $A(\lambda)$ modulation takes place in the near infrared, around the first-order minimum of $R(\lambda)$ where the AR layers increase the amount of light which can be absorbed.

The quantified performance (Table 1) of the YSZ (170 nm)/$V_{0.986}W_{0.014}O_2$ (37 nm)/YSZ (179 nm) coating includes T_{lum} around 64.5% with almost no modulation (higher A_{lum} above T_{tr} is compensated by lower R_{lum}) and ΔT_{sol} of 7.8% (complement of ΔR_{sol} of 3.1% + ΔA_{sol} of −10.9%). The quantified performance of the YSZ (172 nm)/$V_{0.986}W_{0.014}O_2$ (67 nm)/YSZ (182 nm) coating includes T_{lum} around 46.1% with a slight modulation (ΔT_{lum} of 5.1% resulting from ΔA_{lum} of −5.3%) and ΔT_{sol} of 13.2% (complement of ΔR_{sol} of −2.9% + ΔA_{sol} of −10.3%). Note that the energy saving achieved using these coatings which include AR layers is predominantly (at h = 67 nm) or only (at h = 37 nm) due to the absorption (close to the outer window surface, leading to its enhanced blackbody radiation), not due to the reflection. This is

Table 1
The luminous and solar transmittance ($T_{lum}(T_m)$ and $T_{sol}(T_m)$, respectively), reflectance ($R_{lum}(T_m)$ and $R_{sol}(T_m)$, respectively) and absorption ($A_{lum}(T_m)$ and $A_{sol}(T_m)$, respectively) measured at $T_{ms} = -20°C$ and $T_{mm} = 70°C$, together with the corresponding modulations ΔT_{lum}, ΔR_{lum} and ΔA_{lum}, and ΔT_{sol}, ΔR_{sol} and ΔA_{sol} for the YSZ (170 nm)/$V_{0.986}W_{0.014}O_2$ (37 nm)/YSZ (179 nm) coating and the YSZ (172 nm)/$V_{0.986}W_{0.014}O_2$ (67 nm)/YSZ (182 nm) coating on 1 mm thick glass substrates.

h (nm)	T_{lum} (T_{ms}) (%)	T_{lum} (T_{mm}) (%)	ΔT_{lum} (%)	T_{sol} (T_{ms}) (%)	T_{sol} (T_{mm}) (%)	ΔT_{sol} (%)
37	64.3	64.7	−0.4	57.9	50.1	7.8
67	48.6	43.5	5.1	43.5	30.3	13.2
h (nm)	**R_{lum} (T_{ms}) (%)**	**R_{lum} (T_{mm}) (%)**	**ΔR_{lum} (%)**	**R_{sol} (T_{ms}) (%)**	**R_{sol} (T_{mm}) (%)**	**ΔR_{sol} (%)**
37	7.6	4.0	3.6	10.9	7.8	3.1
67	6.4	6.2	0.2	15.9	18.8	−2.9
h (nm)	**A_{lum} (T_{ms}) (%)**	**A_{lum} (T_{mm}) (%)**	**ΔA_{lum} (%)**	**A_{sol} (T_{ms}) (%)**	**A_{sol} (T_{mm}) (%)**	**ΔA_{sol} (%)**
37	28.1	31.3	−3.2	31.2	42.1	−10.9
67	45.0	50.3	−5.3	40.6	50.9	−10.3

contrary to the common knowledge which is relevant for the single VO_2 layers.

The importance of AR layers for the coating performance is further illustrated in Fig. 8, where the aforementioned T_{lum} and ΔT_{sol} values are compared with those measured before the deposition of the top second-order AR layer. The addition of this overlayer improves T_{lum} from 50.2% to 64.5% (at $h = 37$ nm) or from 40.9% to 46.1% (at $h = 67$ nm), and at the same time it improves ΔT_{sol} from 5.7% to 7.8% (at $h = 37$ nm) or from 8.9% to 13.2% (at $h = 67$ nm). Although this improvement is large, the finite k of the top YSZ layer (Fig. 2) makes it only the lower bound of the achievable one.

Fig. 9 compares the performance of both presented sputtered coatings (Table 1) with that of other VO_2-based thermochromic coatings prepared by various sputtering techniques in various laboratories. Let us emphasize that the figure captures all the key criteria of success: T_{lum}, ΔT_{sol}, T_{tr} and maximum substrate temperature. This is unlike that part of the literature where the research and the evaluation of its results is focused on an improvement of only some of these quantities at the cost of the other ones, or where some of these quantities such as T_{tr} are not reported at all. The figure takes into account only those sputtered coatings which exhibit $T_{tr} \leq 38$ °C. In the $V_{0.98}W_{0.02}O_2$ (100 nm)/SnO_2(50 nm) and $V_{0.872}Sr_{0.119}W_{0.009}O_2$ (100 nm)/SnO_2(50 nm) coatings, both on quartz glass, the thermochromic VO_2-based layers were deposited using RF magnetron sputtering of a single V–W and V–Sr–W target, respectively, in an argon-oxygen gas mixture at a substrate temperature of 450 °C [20]. The $V_{0.98}W_{0.02}O_2/SnO_2$ coating exhibited $T_{lum} = 35.3\%$ and $\Delta T_{sol} = 6.0\%$ while the $V_{0.872}Sr_{0.119}W_{0.009}O_2/SnO_2$ coating exhibited $T_{lum} = 61.4\%$ and $\Delta T_{sol} = 5.2\%$. The $V_{0.931}Fe_{0.069}O_2$ (145 nm), $V_{0.902}Fe_{0.098}O_2$ (147 nm) and $V_{0.880}Fe_{0.120}O_2$ (148 nm) coatings were prepared on glass (not specified) substrates using DC magnetron sputtering of a single V–Fe target in an argon-oxygen gas mixture at a substrate temperature of 60 °C, with an additional in-situ annealing at 450 °C for 30 min in oxygen [21]. The successive increase in the Fe content from 6.9% to 12.0% resulted in a corresponding increase of T_{lum} from 34.3% to 36.8%, but also in a corresponding decrease of the relatively high ΔT_{sol} from 14.6% to 11.3%. The same process, but with a single V–Fe–Mg sputter target, was applied to prepare the $V_{0.878}Fe_{0.092}Mg_{0.030}O_2$, $V_{0.838}Fe_{0.092}Mg_{0.070}O_2$ and $V_{0.789}Fe_{0.092}Mg_{0.119}O_2$ coatings with a thickness of approximately 150 nm on glass substrates [52]. The successive increase in the Mg content from 3.0% to 11.9% resulted in a corresponding increase of T_{lum} from 42.1% to 48.9%, but also in a corresponding decrease of ΔT_{sol} from 12.8% to 3.9%. For comparison, the values of $T_{lum} = 59.4\%$ and $\Delta T_{sol} = 5.5\%$, and $T_{lum} = 48.0\%$ and $\Delta T_{sol} = 10.4\%$ for the ZrO_2(180 nm)/$V_{0.982}W_{0.018}O_2$ (45 nm)/ZrO_2(180 nm) and ZrO_2(180 nm)/$V_{0.982}W_{0.018}O_2$ (69 nm)/ZrO_2(180 nm) coatings, respectively, prepared on SLG in our laboratories recently [35], are also given in Fig. 9. It can be seen that the presented coating design (in the first place the choice of the template layer) and the industry-friendly low-temperature high-rate deposition technique allowed us to achieve further progress and to move the line representing the h-induced trade-off between T_{lum} and ΔT_{sol} further toward the area of required values denoted in the top right corner. This also constitutes an indirect confirmation that this deposition technique allowed us (once again contrary to claims in part of the literature) to lower T_{tr} by W doping without concessions in terms of T_{lum} and/or ΔT_{sol}.

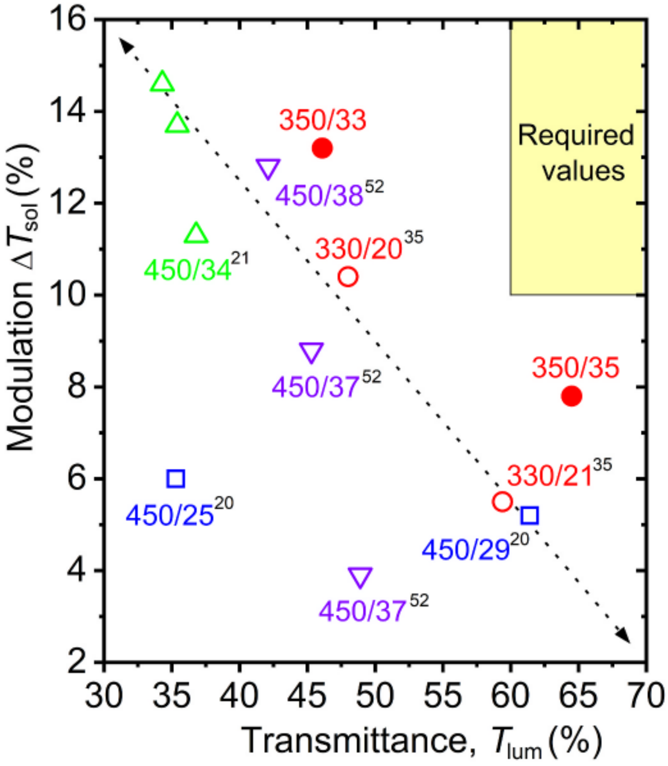

Fig. 9. The average luminous transmittance (T_{lum}) and the modulation of the solar energy transmittance (ΔT_{sol}) achieved in this work (full circles) and reported in the literature [20,21,35,52] (empty symbols) for VO_2-based coatings with a transition temperature $T_{tr} \leq 38°C$ prepared on glass substrates using magnetron sputter deposition. The labels denote a maximum substrate temperature during the preparation (deposition and possible post-annealing) of the coatings and their transition temperature (both in °C), with the reference number in the superscript. The shaded area represents the required values of T_{lum} and ΔT_{sol} for smart-window applications. A trade-off line (dotted) between T_{lum} and ΔT_{sol} for the state-of-the-art coatings is also shown.

4. Conclusions

We have presented and explained a scalable deposition technique for the preparation of high-performance thermochromic YSZ/$V_{0.986}W_{0.014}O_2$/YSZ coatings on soda-lime glass at a relatively low substrate surface temperature (350 °C) and without any substrate bias voltage. The high-rate deposition (53 nm/min at the target-to-substrate distance of 100 mm) of the highly crystalline thermochromic $V_{0.986}W_{0.014}O_2$ layers, containing only the monoclinic VO_2 (M1) and/or the tetragonal VO_2 (R) crystal grains, was performed using a controlled deep oscillation magnetron sputtering of a composite V–W target. The compact antireflection YSZ layers, containing only the tetragonal YSZ crystal grains, were deposited using a controlled standard HiPIMS of a composite Zr–Y target. The YSZ/$V_{0.986}W_{0.014}O_2$/YSZ coatings exhibit a transition temperature of 33–35 °C at $T_{lum} = 64.5\%$ and $\Delta T_{sol} = 7.8\%$ for a $V_{0.986}W_{0.014}O_2$ thickness of 37 nm, and $T_{lum} = 46.1\%$ and $\Delta T_{sol} = 13.2\%$ for a $V_{0.986}W_{0.014}O_2$ thickness of 67 nm. Such a combination of properties, together with the relatively low deposition temperature, has not yet been published by other teams for thermochromic VO_2-based coatings prepared by a deposition technique which is compatible with existing magnetron sputtering systems in glass production lines and in roll-to-roll deposition devices.

CRediT authorship contribution statement

Michal Kaufman: Visualization, Investigation, Data curation. **Jaroslav Vlček:** Writing – review & editing, Writing – original draft, Methodology, Conceptualization. **Jiří Houška:** Writing – review & editing, Writing – original draft. **Radomír Čerstvý:** Investigation. **Sadoon Farrukh:** Investigation. **Mohamed Chargaoui:** Investigation. **Stanislav Haviar:** Investigation. **Jiechao Jiang:** Visualization, Investigation. **Efstathios I. Meletis:** Investigation. **Šimon Kos:** Writing – review & editing.

Declaration of competing interest

The authors declare that they have no known competing financial interests or personal relationships that could have appeared to influence the work reported in this paper.

Data availability

Data will be made available on request.

Acknowledgments

This work was supported by the Czech Science Foundation under Project No. 21-28277S and by the U.S. National Science Foundation under Award No. DMR-2122128.

References

[1] H. Ritchie, M. Roser, P. Rosado, CO2 and greenhouse gas emissions, Our world in data (2020). https://ourworldindata.org/co2-and-other-greenhouse-gas-emissions.
[2] A.M. Omer, Energy, environment and sustainable development, Renewable Sustainable Energy Rev. 12 (2008) 2265–2300.
[3] F.J. Morin, Oxides which show a metal-to-insulator transition at the Neel temperature, Phys. Rev. Lett. 3 (1959) 34–36.
[4] Y. Xue, S. Yin, Element doping: a marvelous strategy for pioneering the smart applications of VO_2, Nanoscale 14 (2022) 11054–11097.
[5] L. Miao, Y. Peng, D. Wang, J. Liang, C. Hu, E. Nishibori, L. Sun, C.A.J. Fisher, S. Tanemura, Characterisation of the temperature-dependent M_1 to R phase transition in W-doped VO_2 nanorod aggregates by Rietveld refinement and theoretical modelling, Phys. Chem. Chem. Phys. 22 (2020) 7984–7994.
[6] G. Sun, X. Cao, X. Li, S. Bao, N. Li, M. Liang, A. Gloter, H. Gu, P. Jin, Low-temperature deposition of VO_2films with high crystalline degree by embedding multilayered structure, Sol. Energy Mater. Sol. Cells 161 (2017) 70–76.
[7] T. Chang, X. Cao, N. Li, S. Long, X. Gao, L.R. Dedon, G. Sun, H. Luo, P. Jin, Facile and low-temperature fabrication of thermochromic Cr_2O_3/VO_2 smart coatings: enhanced solar modulation ability, high luminous transmittance and uv-shielding function, ACS Appl. Mater. Interfaces 9 (2017) 26029–26037.
[8] T.-C. Chang, X. Cao, S.-H. Bao, S.-D. Ji, H.-J. Luo, P. Jin, Review on thermochromic vanadium dioxide based smart coatings: from lab to commercial application, Adv. Manuf. 6 (2018) 1–19.
[9] Y. Zhang, B. Li, Z. Wang, S. Tian, B. Liu, X. Zhao, N. Li, G. Sankar, S. Wang, Facile preparation of $Zn_2V_2O_7$–VO_2 composite films with enhanced thermochromic properties for smart windows, ACS Appl. Electron. Mater. 3 (2021) 2224–2232.
[10] M. Junghähnel, J. Westphalen, Processing on flexible glass-challenges and opportunities, SVC Bull. Fall/Winter (2017) 31–39.
[11] M. Junghähnel, J. Fahlteich, Thin-film deposition on flexible glass by plasma processes, in: S.M. Garner (Ed.), Flexible Glass: Enabling Thin, Lightweight, and Flexible Electronics, first ed., Scrivener Publishing LLC, Beverly, CA, USA, 2017, pp. 129–180.
[12] M. Fahland, O. Zywitzki, T. Modes, K. Vondkar, T. Werner, C. Ottermann, M. Berendt, G. Pollack, Roll-to-roll sputtering of indium tin oxide layers onto ultrathin flexible glass, Thin Solid Films 669 (2019) 56–59.
[13] J.-P. Fortier, B. Baloukas, O. Zabeida, J.E. Klemberg-Sapieha, L. Martinu, Thermochromic VO_2thin films deposited by HiPIMS, Sol. Energy Mater. Sol. Cells 125 (2014) 291–296.
[14] Y.-X. Ji Aijaz, J. Montero, G.A. Niklasson, C.G. Granqvist, T. Kubart, Low-temperature synthesis of thermochromic vanadium dioxide thin films by reactive high power impulse magnetron sputtering, Sol. Energy Mater. Sol. Cells 149 (2016) 137–144.
[15] M. Saeli, C. Piccirillo, I.P. Parkin, R. Binions, I. Ridley, Energy modelling studies of thermochromic glazing, Energy Build. 42 (2010) 1666–1673.
[16] Y. Gao, H. Luo, Z. Zhang, L. Kang, Z. Chen, J. Du, M. Kanehira, C. Cao, Nanoceramic VO_2thermochromic smart glass: a review on progress in solution processing, Nano Energy 1 (2012) 221–246.
[17] L. Hu, H. Tao, G. Chen, R. Pan, M. Wan, D. Xiong, X. Zhao, Porous W-doped VO_2films with simultaneously enhanced visible transparency and thermochromic properties, J. Sol. Gel Sci. Technol. 77 (2015) 85–93.
[18] B. Baloukas, S. Loquai, L. Martinu, VO_2-based thermally active low emissivity coatings, Sol. Energy Mater. Sol. Cells 183 (2018) 25–33.
[19] N. Wang, Q.S. Goh, P.L. Lee, S. Magdassi, Y. Long, One-step hydrothermal synthesis of rare earth/W-codoped VO_2 nanoparticles: reduced phase transition temperature and improved thermochromic properties, J. Alloys Compd. 711 (2017) 222–228.
[20] M.K. Dietrich, F. Kuhl, A. Polity, P.J. Klar, Optimizing thermochromic VO_2 by co-doping with W and Sr for smart window applications, Appl. Phys. Lett. 110 (2017), 141907.
[21] L. Lu, Z. Wu, C. Ji, M. Song, H. Feng, X. Ma, Y. Jiang, Effect of Fe doping on thermochromic properties of VO_2 films, J. Mater. Sci. Mater. Electron. 29 (2018) 5501–5508.
[22] S. Loquai, B. Baloukas, J.E. Klemberg-Sapieha, L. Martinu, HiPIMS-deposited thermochromic VO_2 films with high environmental stability, Sol. Energy Mater. Sol. Cells 160 (2017) 217–224.
[23] T. Chang, X. Cao, L.R. Dedon, S. Long, A. Huang, Z. Shao, N. Li, H. Luo, P. Jin, Optical design and stability study for ultrahigh-performance and long-lived vanadium dioxide-based thermochromic coatings, Nano Energy 44 (2018) 256–264.
[24] S. Long, X. Cao, N. Li, Y. Xin, G. Sun, T. Chang, S. Bao, P. Jin, Application-oriented VO_2 thermochromic coatings with composite structures: optimized optical performance and robust fatigue properties, Sol. Energy Mater. Sol. Cells 189 (2019) 138–148.
[25] N. Shen, S. Chen, Z. Chen, X. Liu, C. Cao, B. Dong, H. Luo, J. Liu, Y. Gao, The synthesis and performance of Zr-doped and W–Zr-codoped VO_2 nanoparticles and derived flexible foils, J. Mater. Chem. A 2 (2014) 15087–15093.
[26] L. Dai, S. Chen, J. Liu, Y. Gao, J. Zhou, Z. Chen, C. Cao, H. Luo, M. Kanehira, F-doped VO_2 nanoparticles for thermochromic energy-saving foils with modified color and enhanced solar-heat shielding ability, Phys. Chem. Chem. Phys. 15 (2013) 11723–11729.
[27] C.G. Granqvist, Recent progress in thermochromics and electrochromics: a brief survey, Thin Solid Films 614 (2016) 90–96.
[28] S. Wang, M. Liu, L. Kong, Y. Long, X. Jiang, A. Yu, Recent progress in VO_2 smart coatings: strategies to improve the thermochromic properties, Prog. Mater. Sci. 81 (2016) 1–54.
[29] M. Li, S. Magdassi, Y. Gao, Y. Long, Hydrothermal synthesis of VO_2 polymorphs: advantages, challenges and prospects for the application of energy efficient smart windows, Small 13 (2017), 1701147.
[30] F. Xu, X. Cao, H. Luo, P. Jin, Recent advances in VO_2-based thermochromic composites for smart windows, J. Mater. Chem. C 6 (2018) 1903–1919.
[31] J. Houska, Design and reactive magnetron sputtering of thermochromic coatings, J. Appl. Phys. 131 (2022), 110901.
[32] S. Loquai, B. Baloukas, O. Zabeida, J.E. Klemberg-Sapieha, L. Martinu, HiPIMS-deposited thermochromic VO_2 films on polymeric substrates, Sol. Energy Mater. Sol. Cells 155 (2016) 60–69.
[33] J.L. Victor, C. Marcel, L. Sauques, N. Penin, A. Rougier, High quality thermochromic VO_2 thin films deposited at room temperature by balanced and unbalanced HiPIMS, Sol. Energy Mater. Sol. Cells 227 (2021), 111113.
[34] J.T. Gudmundsson, On reactive high power impulse magnetron sputtering, Plasma Phys. Contr. Fusion 58 (2015), 014002.
[35] D. Kolenatý, J. Vlček, T. Bárta, J. Rezek, J. Houška, S. Haviar, High-performance thermochromic VO_2-based coatings with a low transition temperature deposited on glass by a scalable technique, Sci. Rep. 10 (2020), 11107.
[36] J. Vlček, D. Kolenatý, J. Houška, T. Kozák, R. Čerstvý, Controlled reactive HiPIMS-effective technique for low-temperature (300 °C) synthesis of VO_2 films with semiconductor-to-metal transition, J. Phys. D Appl. Phys. 50 (2017) 38LT01.
[37] J. Vlček, D. Kolenatý, T. Kozák, J. Houška, J. Čapek, Š. Kos, Ion-flux characteristics during low-temperature (300 °C) deposition of thermochromic VO_2 films using controlled reactive HiPIMS, J. Phys. D Appl. Phys. 52 (2019), 025205.
[38] J. Vlček, J. Rezek, J. Houška, T. Kozák, J. Kohout, Benefits of the controlled reactive high-power impulse magnetron sputtering of stoichiometric ZrO_2films, Vacuum 114 (2015) 131–141.

[39] J. Houska, D. Kolenaty, J. Vlcek, T. Barta, J. Rezek, R. Cerstvy, Significant improvement of the performance of $ZrO_2/V_{1-x}W_xO_2/ZrO_2$ thermochromic coatings by utilizing a second-order interference, Sol. Energy Mater. Sol. Cells 191 (2019) 365–371.

[40] J. Rezek, J. Szelwicka, J. Vlček, R. Čerstvý, J. Houška, M. Fahland, J. Fahlteich, Transfer of the sputter technique for deposition of strongly thermochromic VO_2-based coatings on ultrathin flexible glass to large-scale roll-to-roll device, Surf. Coat. Technol. 442 (2022), 128273.

[41] F. Ferreira, C. Sousa, A. Cavaleiro, A. Anders, J. Oliveira, Phase tailoring of tantalum thin films deposited in deep oscillation magnetron sputtering mode, Surf. Coat. Technol. 314 (2017) 97–104.

[42] J. Lin, High rate reactive sputtering of Al_2O_3 coatings by HiPIMS, Surf. Coat. Technol. 357 (2019) 402–411.

[43] K. Okimura, J. Sakai, Changes in lattice parameters of VO_2 films grown on c-plane Al_2O_3 substrates across metal–insulator transition, Jpn. J. Appl. Phys. 48 (2009), 045504.

[44] Y. Yang, Y. Yao, B. Zhang, H. Lin, Z. Luo, C. Gao, C. Zhang, C. Kang, Investigating metal–insulator transition and structural phase transformation in the (010)-VO_2/(001)-YSZ epitaxial thin films, Materials 11 (2018) 1713.

[45] P. Kudláček, J. Vlček, K. Burcalová, J. Lukáš, Highly ionized fluxes of sputtered titanium atoms in high-power pulsed magnetron discharges, Plasma Sources Sci. Technol. 17 (2008), 025010.

[46] T. Kozák, J. Vlček, A parametric model for reactive high-power impulse magnetron sputtering of films, J. Phys. D Appl. Phys. 49 (2016), 055202.

[47] J. Vlček, M. Kaufman, A.D. Pajdarová, S. Haviar, R. Čerstvý, J. Houška, M. Farahani, Detailed pathway for a fast low-temperature synthesis of strongly thermochromic W-doped VO_2 films with a low transition temperature, J. Phys. D Appl. Phys. 56 (2023) 505301.

[48] **Available online:** http://rredc.nrel.gov/solar/spectra/am1.5/. (Accessed 14 June 2016) http://hyperphysics.phy-astr.gsu.edu/hbase/vision/efficacy.html.

[49] The International Centre for Diffraction Data, PDF-4+ Database; The International Centre for Diffraction Data: Newtown Square, PA, USA, 2022.

[50] J.C. Jiang, T. Bárta, J. Vlček, J. Houška, E.I. Meletis, Microstructure of high-performance thermochromic $ZrO_2/V_{0.984}W_{0.016}O_2/ZrO_2$ coating with a low transition temperature (22° C) prepared on flexible glass, Surf. Coat. Technol. 424 (2021), 127654.

[51] J. Houska, D. Kolenaty, J. Rezek, J. Vlcek, Characterization of thermochromic VO_2 (prepared at 250° C) in a wide temperature range by spectroscopic ellipsometry, Appl. Surf. Sci. 421 (2017) 529–534.

[52] fish 0,punct]">C. Ji, Z. Wu, L. Lu, X. Wu, J. Wang, X. Liu, H. Zhou, Z. Huang, J. Gou, Y. Jiang, High thermochromic performance of Fe/Mg co-doped VO_2thin films for smart window applications, J. Mater. Chem. C 6 (2018) 6502.